Periodic Rotor-Blade Aerodynamics Including Loading Effects

Steven R. Manwaring* and Sanford Fleeter†
Purdue University, West Lafayette, Indiana 47907

A series of experiments are performed to investigate and quantify the effects of steady aerodynamic loading on the unsteady gust aerodynamics of a first-stage rotor blade at realistic values of the reduced frequency. These are accomplished in an extensively instrumented axial flow research compressor with the high-reduced frequency gusts generated by the wakes from the inlet guide vanes. The unsteady pressure response on the low-camber blade pressure surface is primarily affected by mean flow incidence angle except in the accelerating mean flowfield of the front chord region at negative incidence. However, the unsteady pressure response on the high-camber suction surface is affected by steady loading over the entire surface, i.e., gust interactions with the accelerating mean flowfield in the front half and the large viscous regions in the aft half. The multistage effects associated with compressor rotor-stator blade-row operation in the super-resonant flow regime, wherein acoustic waves propagate, are also considered. The unsteady pressure difference and thus, the unsteady lift, due to acoustic waves generated by the downstream super-resonant, rotor-stator interaction, is nearly zero, even though the individual surface unsteady pressures are of relatively large amplitude.

Nomenclature

C = rotor chord
$\bar{C}_\ell$ = steady lift coefficient, $\int_0^C (\bar{p}_p - \bar{p}_s)\, dx/\frac{1}{2}\rho U_t^2 C$
C_p = first harmonic unsteady pressure coefficient
$\bar{C}_p$ = static pressure coefficient
$C_{\Delta p}$ = first harmonic unsteady pressure difference
$\bar{i}$ = mean incidence angle
k = reduced frequency, $\omega C/2\bar{V}_x$
$\bar{p}$ = rotor-surface static pressure
$\bar{p}_{\text{exit}}$ = rotor-exit static pressure
$\hat{p}$ = first harmonic complex unsteady pressure
$\hat{u}^+$ = first harmonic streamwise gust component
U_t = blade tip speed
$\hat{v}^+$ = first harmonic transverse gust component
$\bar{V}_x$ = mean axial velocity
$\bar{\beta}$ = rotor relative mean flow angle
σ = interblade phase angle
ω = inlet guide vane (IGV) passing frequency

Introduction

PERIODIC aerodynamic excitations generate unsteady aerodynamic forces and moments on turbomachinery blading. When the aerodynamic excitation frequency corresponds to a blade natural frequency, catastrophic vibrational responses may occur. The operating conditions at which these resonance conditions are found can be predicted with Campbell diagrams. However, accurate predictions of the amplitude of the resonant blade vibration cannot currently be made due to the inability of mathematical models to accurately analyze the aerodynamic forcing function and the resulting unsteady aerodynamics acting on the blading.

Wakes shed by upstream airfoil rows are the most common aerodynamic excitation source (see Fig. 1). On a first principles basis, the resulting high-reduced frequency forced response problems are analyzed by first defining the unsteady aerodynamic forcing function in terms of its harmonics. The periodic response of the airfoil row to each harmonic is then assumed to include two components. The first is due to the parallel and normal components of the harmonic forcing function being swept past the nonresponding airfoil row, termed the streamwise (parallel) and transverse (normal) gust responses, respectively. The second, the self-induced, unsteady aerodynamics, arises when the aerodynamic forcing function generates a vibrational response of the airfoils.

Mathematical models to predict the unsteady aerodynamic response of an airfoil row to a gust are being developed. Small perturbation thin airfoil analyses were considered initially with integral solutions obtained for the unsteady lift on a flat plate airfoil cascade at zero incidence in an inviscid, irrotational flowfield, for example, Refs. 1–4. Models that consider the profile of the airfoil as well as finite incidence angles have subsequently been developed. Goldstein and Atassi[5] and Atassi[6] analyzed the inviscid, incompressible flow past an isolated airfoil of arbitrary shape at finite angle of attack subject to an interacting gust. Chiang and Fleeter[7] utilized the complete first-order model and a locally analytical solution technique to predict the unsteady loading on a cascade of thick, cambered airfoils at nonzero incidence angles in an incompressible flow due to a convected gust.

Unsteady aerodynamic gust experiments of direct interest to turbomachines have been performed in low-speed research compressors at both high and low values of the reduced frequency. The effects of airfoil camber, rotor-stator axial spacing, and the waveform of the aerodynamic forcing function have been investigated on the stationary vane rows of both single and multistage compressors.[8–11] The aerodynamic forcing function in these experiments was made up of the high-reduced frequency wakes shed by the upstream rotor blades. Hardin et al.[12] measured low-reduced frequency oscillating airfoil aerodynamics on a rotor of a single-stage, low-speed compressor and also stated that they had performed distortion gust response experiments, although they did not present these results.

In this paper, the fundamental flow physics of rotor-blade row unsteady gust aerodynamics are experimentally investigated at realistic high values of the reduced frequency for the

Received Aug. 22, 1988; revision received July 24, 1989.

*AFRAPT Trainee, Thermal Sciences and Propulsion Center, School of Mechanical Engineering.
†Professor and Director, Thermal Sciences and Propulsion Center, School of Mechanical Engineering.

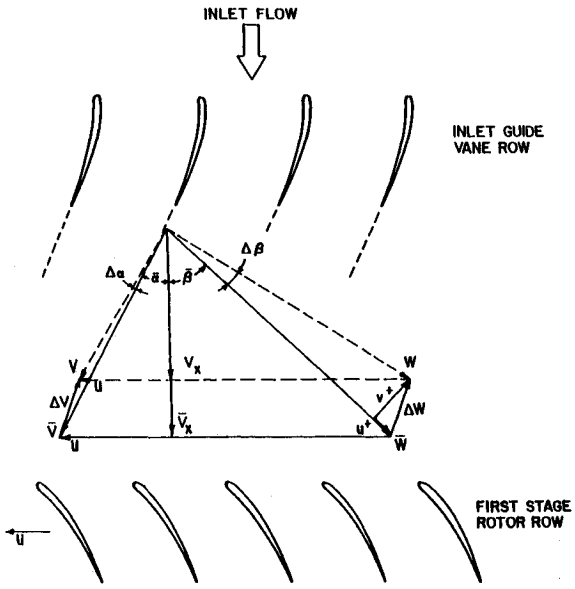

Fig. 1 Rotor-blade row inlet flowfield.

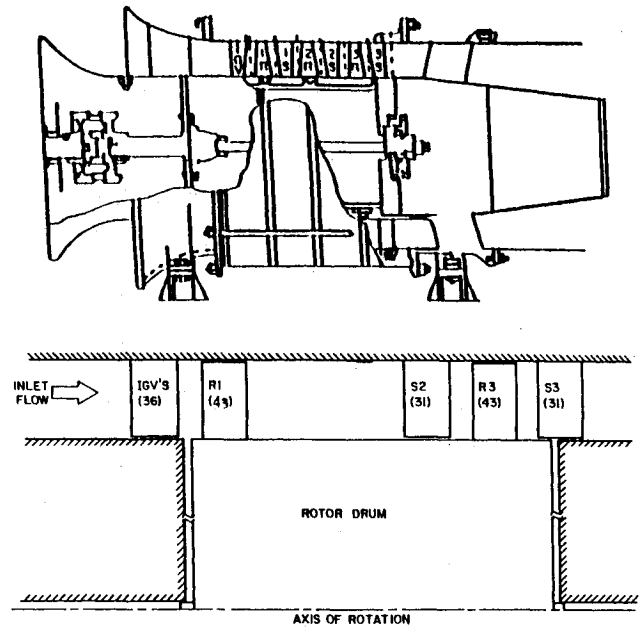

Fig. 2 Baseline compressor configuration.

Table 1 Overall airfoil and compressor characteristics

	Rotor	Stator	IGV
Airfoil type	C4	C4	C4
Number of airfoils	43	31	36
Chord, C, mm	30	30	30
Solidity, C/S	1.14	1.09	0.96
Camber, θ	28.0	27.7	36.9
Stagger angle, γ	36.0	−36.0	21.0
Aspect ratio	2.0	2.0	2.0
Thickness/chord, %	10.0	10.0	10.0
Flow rate, kg/s		2.03	
Design axial velocity, m/s		24.4	
Design rotational speed, RPM	2250		
Number of stages		3	
Design stage pressure ratio		1.0	
Inlet tip diameter, mm		420	
Hub/tip radius ratio		0.714	
Stage efficiency, %		85	

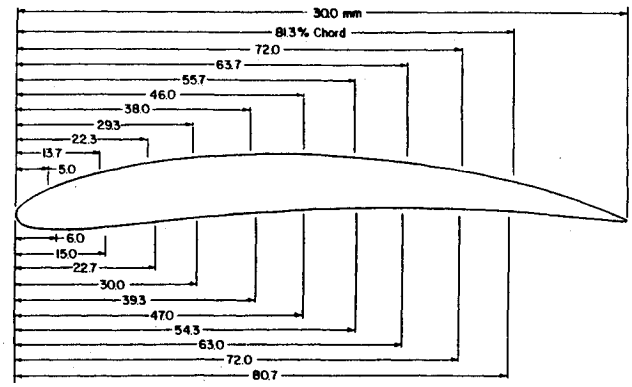

Fig. 3 Rotor-blade profile and instrumentation locations.

first time. In particular, a series of experiments are performed in an extensively instrumented axial flow research compressor to investigate the effects of steady aerodynamic loading on the unsteady gust aerodynamics of a first-stage rotor blade with the high-reduced frequency gusts generated by the wakes from the inlet guide vanes (IGV). The multistage effects associated with operation in the super-resonant flow regime wherein acoustic waves propagate are also considered.

Research Compressor

The Purdue Axial Flow Research Compressor experimentally models the fundamental aerodynamic phenomena inherent in turbomachinery airfoil rows including the airfoil incidence angles, the velocity and pressure variations, the aerodynamic forcing function, the reduced frequency, and the unsteady blade and vane row interactions. The three-stage compressor is driven by a 15-HP dc electric motor and is operated at a speed of 2250 rpm. Each identical stage of the baseline compressor contains 43 rotor-blades and 31 stator vanes having a British C4 profile with the first-stage rotor inlet flowfield established by a row of 36 variable setting IGVs. The overall airfoil and compressor characteristics are presented in Table 1. For these experiments, the first-stage rotor-blade row is extensively instrumented. Because of the large axial gap between the IGV row and the first-stage rotor row, approximately 74% of vane chord, the potential flow effects from the IGV row are negligible and the rotor-row periodic disturbances are due only to the vane viscous wakes. To eliminate potential flow effects from the downstream stator vane row on the instrumented first-stage rotor-blades, the first-stage stators and second-stage rotors are removed, as schematically depicted in Fig. 2.

Instrumentation

Both steady and unsteady data are required. The steady data define the chordwise distribution of the rotor-blade surface static pressure. The unsteady data quantify both the unsteady aerodynamic forcing function to the first-stage rotor and the resulting chordwise distribution of the unsteady pressure on the rotor-blade surfaces.

The detailed steady aerodynamic loading on the rotor-blade surfaces is measured with a chordwise distribution of 20 midspan static pressure taps, 10 on each surface (see Fig. 3). The static pressure at the rotor-exit plane, measured with a rotor-drum static tap, is used as the blade surface static pressure reference. These static pressure measurements are made using a rotor-based, 48-port, constant-speed-drive Scanivalve system located in the rotor drum.

The unsteady aerodynamic forcing function to the instrumented first-stage rotor-blade row, i.e., the exit flowfield of

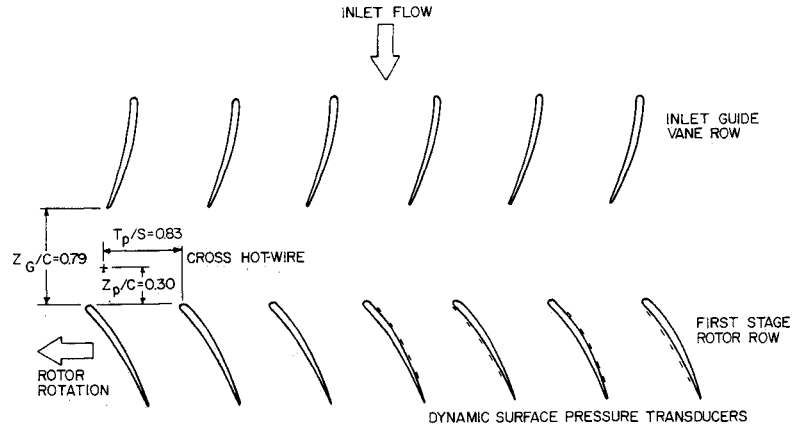

Fig. 4 Schematic of rotating time-variant instrumentation.

the IGVs is measured with a cross hot-wire probe mounted in the rotor frame of reference. The probe is circumferentially located 2.83 blade spacings from the instrumented rotor-blades and 30% of blade chord upstream of the rotor-leading-edge plane as schematically shown in Fig. 4. It is angularly aligned to obtain rotor-relative velocity and flow angle data. The hot wires are calibrated for velocities from 9.1 m/s to 53.4 m/s and ± 35 deg angular variation with the accuracy of the velocity magnitude and angle being 4% and ± 1 deg, respectively.

The measurement of the midspan rotor-blade surface unsteady pressures is accomplished with 20 ultraminiature, high-response transducers embedded in the rotor-blade surfaces at the same chordwise locations as the static pressure taps. Because of blade space limitations, only five transducers are fitted per blade surface and, thus, four instrumented blades, mounted in the rotor row as shown in Fig. 4, are utilized to obtain the 20 unsteady pressure measurements. To minimize the possibility of flow disturbances associated with the inability of the transducer diaphragm to exactly maintain the surface curvature of the blade, a reverse mounting technique is utilized. The pressure surface of one blade and the suction surface of the adjacent blade are instrumented, with transducers embedded in the nonmeasurement surface and connected to the measurement surface by a static tap. The embedded dynamic transducers were both statically and dynamically calibrated. The static calibrations showed good linearity and no discernible hysteresis. The dynamic calibrations demonstrated that the frequency response, in terms of gain attenuation and phase shift, was not affected by the reverse mounting technique. The accuracy of the unsteady pressure measurements, determined from the calibrations, is ± 4%.

The rotating frame-of-reference data signals, i.e., the signals from: 1) the rotor-based Scanivalve static pressure transducer, 2) the 20 rotor-blade surface dynamic pressure transducers, and 3) the cross hot-wire probe are transferred to the stationary reference frame by means of a 40-channel slip ring assembly. Onboard signal conditioning is performed to maintain a good signal-to-noise ratio through the slip rings. The remaining 17 channels of the slip-ring assembly are used to provide excitation to the transducers and excitations and on/off switching to the rotor-based Scanivalve dc motor.

Data Acquisition and Analysis

The rotor-blade surface static pressure data, measured with the rotor-based Scanivalve system, are defined by a root-mean-square error analysis of 20 signal samples with a 95% confidence interval. The reference for these midspan blade pressure measurements is the static pressure at the exit of the rotor, measured on the rotor drum. Thus, the blade surface and the reference static pressures are measured at different

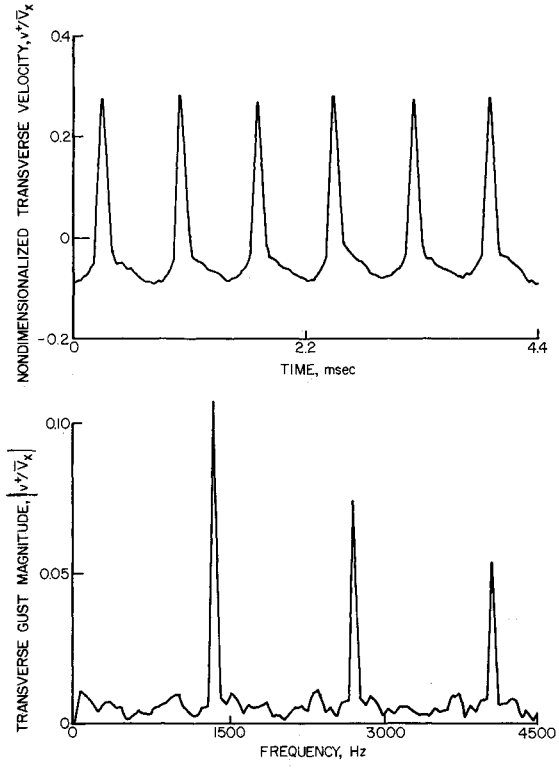

Fig. 5 Periodic transverse velocity and gust entering rotor row.

radii. To account for the resulting difference in the centrifugal forces acting on the air in the static pressure tubing, a correction is applied in calculating the values of the airfoil surface static pressure coefficient defined in Eq. (1)

$$\bar{C}_p = \frac{\bar{p} - \bar{p}_{\text{exit}}}{\frac{1}{2}\rho U_t^2} \tag{1}$$

where U_t is the rotor-blade tip speed.

The unsteady data of primary interest are the first harmonic component of the aerodynamic forcing function, i.e., the unsteady rotor inlet flowfield together with the resulting rotor-blade surface first harmonic unsteady pressures and pressure differences. These are determined by defining a digitized ensemble-averaged unsteady aerodynamic data set consisting of the rotating hot-wire and surface pressure transducer signals at each steady operating point. In particular, these time-variant signals are digitized with a high-speed analog-digital (A/D) system and then ensemble averaged. The key to this

averaging technique is the ability to sample data at a preset time, accomplished by an optical encoder mounted on the rotor shaft. The microsecond range step voltage signal from the encoder is the data initiation time reference and triggers the high-speed A/D multiplexer system. To reduce significantly the random fluctuations superimposed on the periodic signals of interest, 200 averages are used. A Fast Fourier Transform (FFT) algorithm is then applied to these ensemble-averaged signals, and the first harmonic component of the unsteady aerodynamic forcing function, the gust, and the resulting rotor-blade surface, unsteady pressures are determined.

The unsteady inlet flow to the rotor row is measured with the rotating cross hot-wire probe, which quantifies the relative velocity and flow angle. The velocity triangle relations depicted in Fig. 1 are then used to determine the inlet flowfield to the rotor, in particular, the first harmonics of the streamwise and transverse gust components $\hat{u}^+$ and $\hat{v}^+$, respectively. To account for the development of the IGV wakes from the rotating hot-wire measurement location upstream of the rotor-blade row to the rotor-leading-edge plane, the wake similarity and decay model of Lakshminarayana and Davino[13] is utilized.

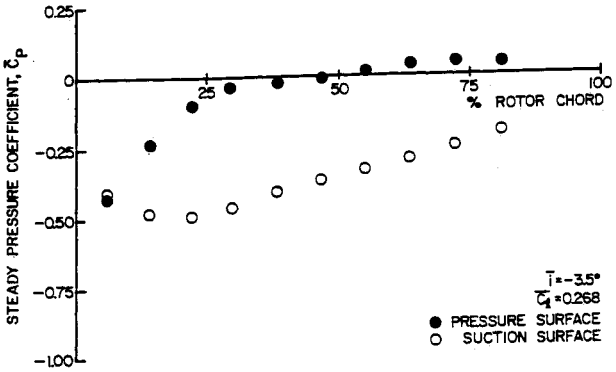

Fig. 6 Blade surface static pressure at low steady loading.

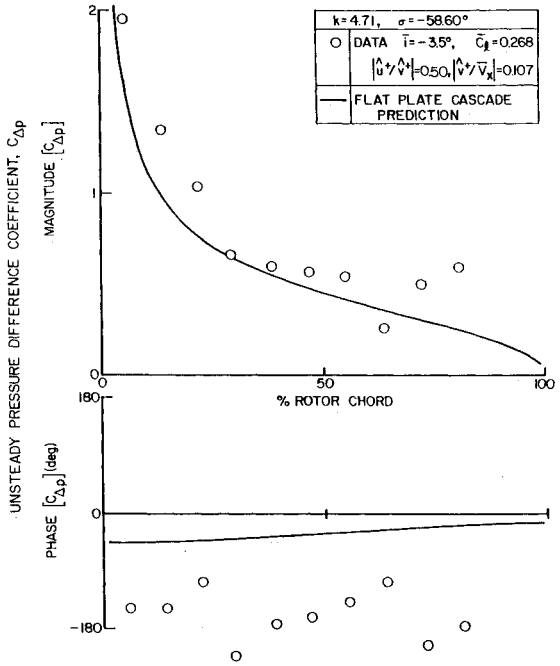

Fig. 7 Baseline blade unsteady pressure difference.

The rotor-blade surface unsteady pressure data, measured with the embedded high-response pressure transducers, are analyzed to determine the first harmonics of the chordwise distribution of the unsteady pressure coefficient C_p and the unsteady pressure difference coefficient, $C_{\Delta p}$. These are defined in Eqs. 2 and are specified from the Fourier coefficients of the digitized blade surface unsteady pressure signals.

$$C_p = \frac{\hat{p}}{\rho \bar{V}_x^2 \left(\frac{\hat{v}^+}{\bar{V}_x}\right) \bar{\beta}} \tag{2a}$$

$$C_{\Delta p} = (C_p)_{\text{pressure}} - (C_p)_{\text{suction}} \tag{2b}$$

where $\hat{p}$ is the first harmonic complex unsteady pressure, $\hat{v}^+$ is the first harmonic complex transverse gust component, $\bar{V}_x$ is the mass-averaged axial velocity, and $\bar{\beta}$ is the relative mean flow angle.

The gust generated rotor-blade row unsteady aerodynamics are presented in the form of chordwise distributions of the first harmonic, complex harmonic pressure and pressure difference coefficients. Also included as a reference where appropriate are predictions from the transverse gust analysis of Smith.[4] This model analyzes the unsteady aerodynamics generated on a flat plate airfoil cascade at zero incidence by a harmonic transverse gust convected with an inviscid, irrotational, subsonic compressible flow.

Results

To investigate and quantify the effects of steady aerodynamic loading on the unsteady gust aerodynamics of a first-stage rotor blade at realistic values of the reduced frequency, a series of experiments are performed. The high-reduced frequency aerodynamic forcing function to the rotor blades is made up of the wakes from the IGVs. Figure 5 presents a sample of the transverse periodic unsteady velocity generated by the IGV wakes and obtained from the rotating cross hot-wire measurement digitized at a rate of 100 kHz. The frequency content of this signal is also demonstrated by the Fourier components, determined by means of a FFT algorithm. The multistage effects associated with operating in the super-resonant flow regime wherein acoustic waves propagate are also considered.

Baseline

The baseline steady and gust-generated, time-variant data for the investigation of the effect of steady loading on rotating blade-row unsteady aerodynamics are obtained at a compressor operating condition corresponding to a low level of steady rotor-blade aerodynamic loading. This also most closely corresponds to the reference transverse gust model, which considers a flat plate airfoil cascade and, thus, no steady loading. For this compressor configuration, this lowest loading condition is defined by a first-stage rotor-blade row mean incidence angle of -3.5 deg. The chordwise distribution of the blade surface static pressure coefficient is presented in Fig. 6.

The first harmonic, gust-generated, unsteady pressure difference coefficient data, with the transverse gust flat plate cascade prediction as a reference, are presented in Fig. 7. Overall, the magnitude data exhibit fair correlation with the prediction with the data increased in value relative to the prediction over the front and midchord regions of the blade. Also, the aft three chordwise data points increase in a somewhat linear fashion, contrary to the trend of the prediction. The correlation of the phase data with the prediction is relatively poor, with the differences being on the order of 90 deg over the entire chord. These differences between the complex unsteady pressure difference data and the flat plate predictions are associated with the airfoil profile and nonzero mean incidence, i.e., the steady loading, as will be discussed in the next section.

Steady Loading Effects

The effect of steady aerodynamic loading, characterized by the mean incidence angle, on the rotor-blade surface static pressure coefficient is shown in Fig. 8. The level of steady loading only affects the static pressure distribution on the rotor-blade pressure surface over the front 40% of the chord. On the suction surface, the variation in the steady loading has a large effect on the static pressure distribution over the entire chord. Also, these data exhibit no indication of steady flow separation.

The effect of steady aerodynamic loading level on the first harmonic, complex, unsteady pressure coefficient on the rotor-blade pressure surface is shown in Fig. 9. The form of the dimensionless unsteady pressure coefficient specified in Eq. (2a) results in a compression of the unsteady pressure magnitude data over the entire pressure surface for all but the two lowest steady loading levels. For these two loading cases, large variations are found in the magnitude data in the neighborhood of the quarter chord. This corresponds to the previously noted effects of steady loading on the rotor-blade surface static pressure wherein loading primarily influenced the front part of the pressure surface. In particular, the static pressure coefficient value for the hub static pressure coefficient upstream of the rotor row is approximately -0.24, thereby indicating that the mean flowfield accelerates around the pressure surface leading edge before decelerating (diffusing) for the two lowest mean incidence angles, i.e., the static pressure coefficient decreases and then increases. Similar to the magnitude data, the effects of steady loading on the pressure surface unsteady pressure phase collapse into approximately one curve with the exception being the lowest steady loading level in the front chord region.

In summary, for the chordwise region where the mean flowfield does not accelerate, i.e., the mid-to-aft chord region for all steady loading levels and the front chord region for the three high steady loading levels, the data compress for all gust amplitude ratios, which indicates that steady loading as characterized by the mean flow incidence is a key mechanism for the low-camber pressure surface unsteady aerodynamic wake response. However, in an accelerating mean flowfield, i.e., the front chord region for the two low steady loading levels, mean flowfield interactions with the unsteady gust are also important.

The entire suction surface unsteady pressure chordwise distribution, both magnitude and phase, is affected by the level of the steady aerodynamic loading (see Fig. 10). Again, this corresponds to the previously presented suction surface static pressure data variation with mean incidence angle. In particular, the front-to-mid-chord region data show a decreasing-increasing magnitude trend with chord with the minimum magnitude chordwise location moving forward with increasing steady loading. This minimum corresponds to the minimum in the static pressure chordwise distribution (see Fig. 8), wherein the chordwise location of the change from accelerating to decelerating mean flow moves forward with increasing mean incidence. Thus, similar to the pressure surface unsteady response in the front chord region at negative mean incidence flow, the unsteady gust interacts with the accelerating mean flowfield around the suction surface in the front chord region. In the mid-to-aft chord, a second decreased magnitude region occurs, with the minimum moving forward with increased mean incidence. In the suction surface aft chord region, where the boundary layer and other viscous effects are at their greatest due to the severe adverse pressure gradient, the gust interaction with this mean flowfield most likely causes the decreasing-increasing magnitude trend shown. As the mean flow incidence angle is increased, i.e., steady loading increases, the aft

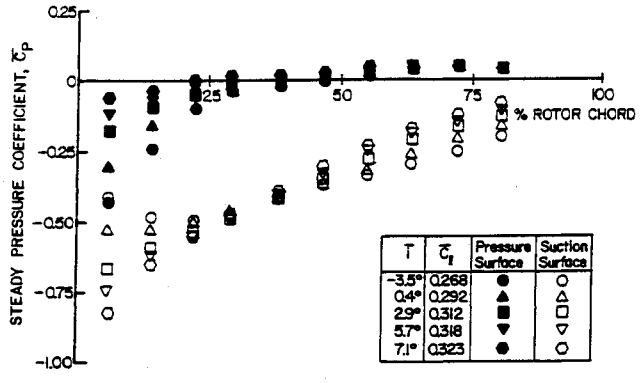

Fig. 8 Steady loading effect on blade surface static pressure.

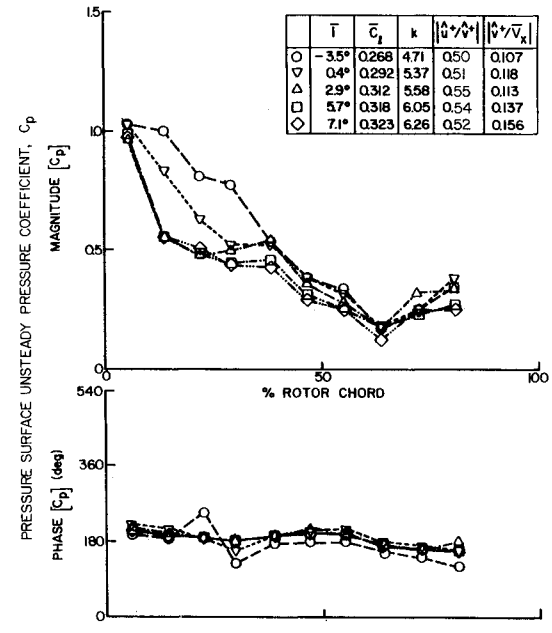

Fig. 9 Loading effect on rotor-blade pressure, surface unsteady pressure.

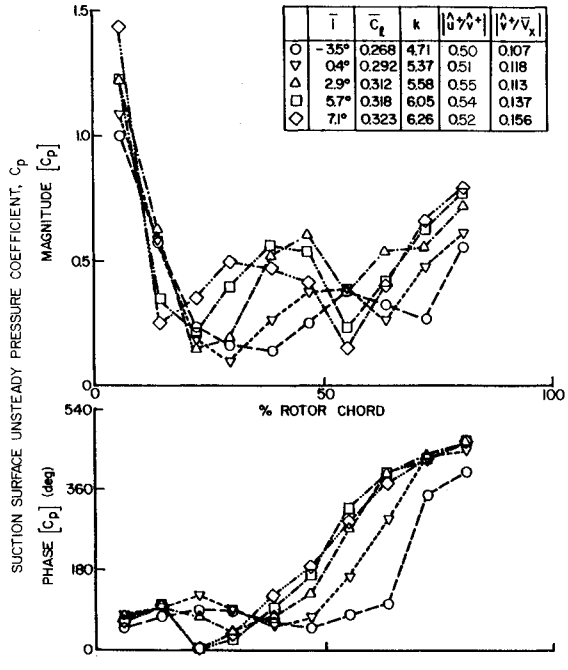

Fig. 10 Loading effect on rotor-blade suction surface unsteady pressure.

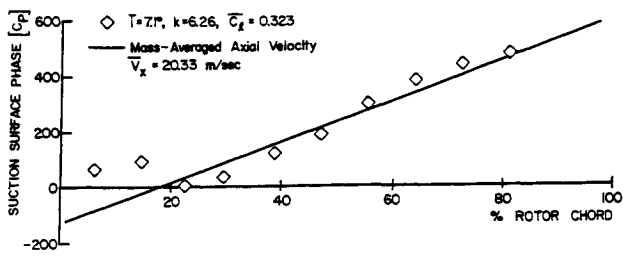

Fig. 11 Chordwise distribution of suction surface phase data at high loading.

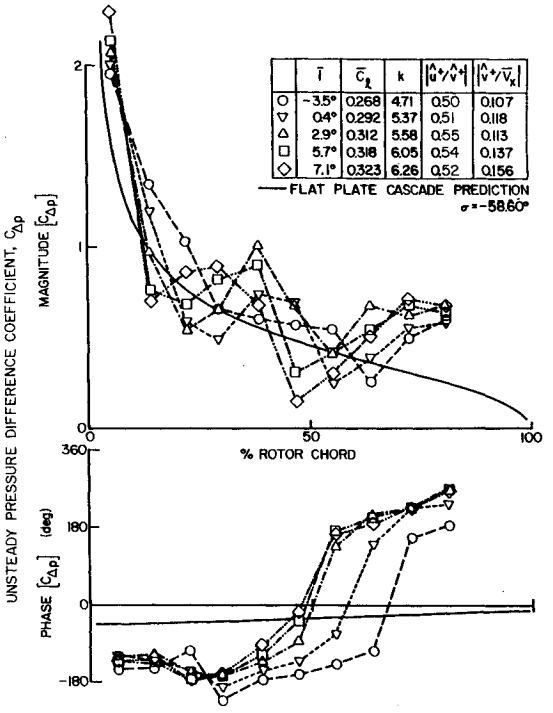

Fig. 12 Loading effect on blade unsteady pressure difference.

suction surface diffusion rate increases and, thus, the large viscous effects move forward, similar to the magnitude minimum trends discussed above. However, verification of this hypothesis cannot be made, with this requiring substantially increased unsteady flow instrumentation to obtain detailed boundary layer and completed unsteady flowfield data.

The steady loading level primarily affects the phase data on the aft three quarters of the rotor-blade suction surface. As the mean incidence angle is increased from the baseline low-loading condition, the chordwise variation of the phase data on the aft part of the suction surface becomes linear, with the extent of this linear distribution increasing with increasing mean incidence. This linear chordwise distribution of the phase data indicates the existence of a convected wave phenomena. This is more clearly demonstrated in Fig. 11, wherein the highest steady loading level suction surface phase data are replotted together with the linear phase curve corresponding to the mass-averaged axial velocity convection time lag. As seen, the wave on the suction surface is convected at approximately the mean axial velocity of the flow through the rotor-blade row. Other authors[8,14] have noted this linear phase distribution corresponding to the mean axial velocity. However, the physical explanation of this wave phenomenon could not be made. This wave phenomenon is related to the gust interacting with the large viscous effects along the suction surface mid-to-aft chord. However, once again, until detailed measurements are made, but this cannot be verified.

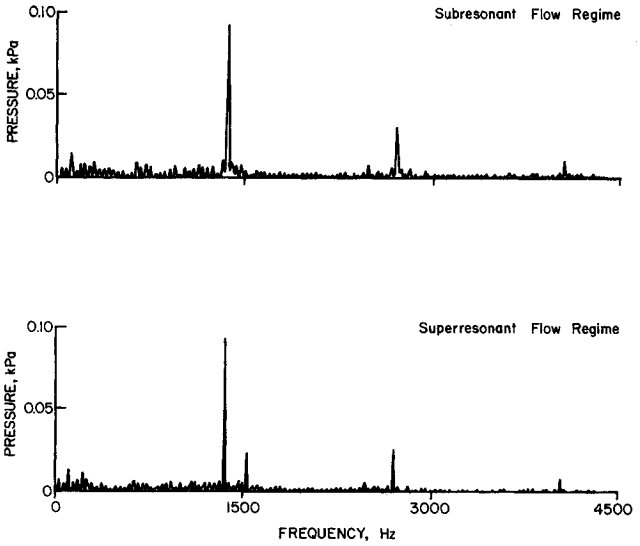

Fig. 13 Harmonic content variation with number of stators in downstream rows.

In summary, on this high-camber suction surface, the steady loading affects the interaction between the mean flowfield and the unsteady gust and, thus, the unsteady aerodynamic response over the entire blade surface. On the front half of the surface, an accelerating mean flowfield affects the unsteady pressure gust response, whereas on the aft half of the surface, large boundary-layer viscous effects affect the unsteady pressure gust response.

The variation of the complex, unsteady pressure difference coefficient data with steady loading level is shown in Fig. 12. The effects of loading on the previously presented individual pressure and suction surface magnitude and phase data are still apparent with the suction surface effects being dominant. For example, analogous to the loading trends on the suction surface, the unsteady difference magnitude data show two decreased magnitude regions, one in the front chord region and the other in the mid-to-aft chord region, with the chordwise location of the magnitude minimums moving forward with increased steady loading. Also, the extent of the increased difference magnitude data on the aft portion of the blade increases with increased steady loading. The difference phase data remain nearly constant over the front portion of the blade. The chordwise location where the rapid increase in the value of the phase data begins to occur moves forward with increasing steady loading. The increased steady loading causes the chordwise distribution of the difference magnitude and phase data to differ greatly from the prediction with the magnitude data not just decreasing with increasing chord and the phase data not remaining nearly constant with chord per the predictions. Thus, to accurately predict the gust generated unsteady loading, the physical unsteady flow effects discussed in the previous blade surface sections must be adequately modeled.

Super-Resonant Flow Regime

The physical description of an acoustic stator-rotor interaction given in Ref. 15 clearly explains the acoustic environment in which resonant conditions occur. The configurations for which subresonant and super-resonant conditions occur for these experiments are described below. The compressor configuration utilized for the above described steady loading experiments had 43 blades in both rotor rows and 31 vanes in each far downstream stator row (see Fig. 2). This corresponds to a subresonant condition wherein the acoustic waves generated by the downstream rotor-stator interactions do not propagate appreciably upstream and, thus, the first-stage rotor row is not affected by the downstream rotor-stator interactions. A

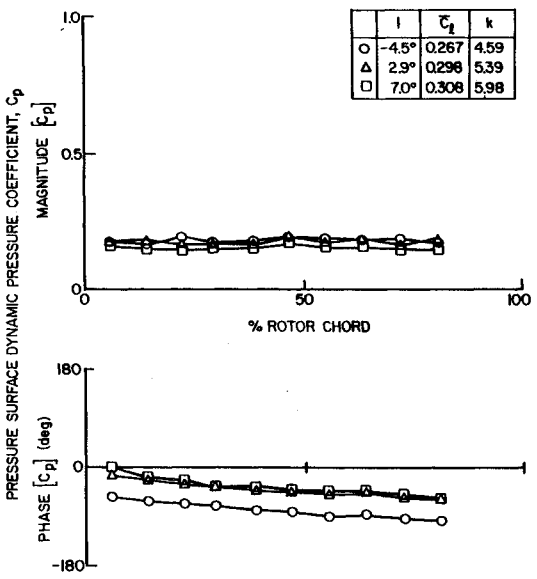

Fig. 14 Blade pressure surface unsteady data at acoustic wave frequency.

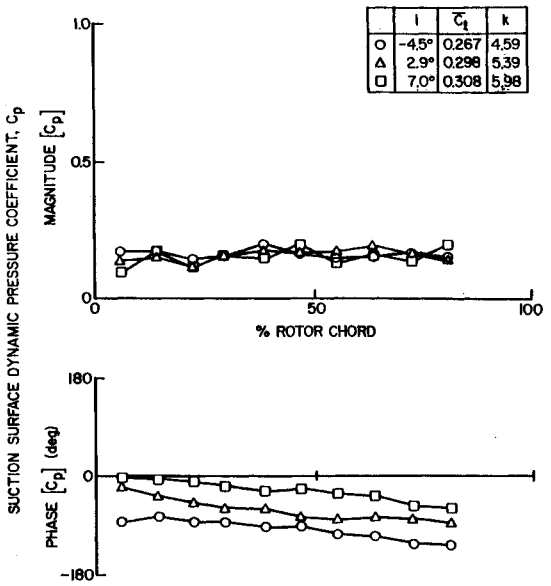

Fig. 15 Blade suction surface unsteady pressure data at acoustic wave frequency.

super-resonant condition was also established in the compressor, accomplished by altering the number of vanes in each stator row. In particular, the number of blades in each rotor row was held constant at 43 with the number of stator vanes changed to 41 vanes per stator row. In this configuration, acoustic waves generated by the downstream rotor-stator interactions propagate upstream to the instrumented first-stage rotor-blade row.

With the compressor operating in a downstream rotor-stator interaction super-resonant flow regime generated with 41 vanes per stator row and 43 blades per rotor row, the upstream propagating acoustic wave could not be detected by the rotating cross hot wire located upstream of the first-stage rotor row. Therefore, to demonstrate the relative amplitude of the downstream generated acoustic wave, Fig. 13 shows the Fourier decomposition of the signal from the first-stage rotor-blade suction surface pressure transducer located nearest the leading edge for both the subresonant condition and the super-resonant conditions. Clearly seen is the relatively large amplitude acoustic wave generated by the downstream rotor-stator interactions. In particular, in the super-resonant condition with 41 vanes per stator row, the transducer signal contains a component at a frequency of 1537.5 Hz that 1) is not seen in the baseline subresonant data obtained with 31 vanes per stator row and 2) has approximately one-fourth the amplitude of that at the IGV wake passing frequency.

The resulting first harmonic, complex, unsteady pressure data on the pressure and suction surfaces of the first-stage rotor-blade row generated by the propagating acoustic wave at three steady loading levels are shown in Figs. 14 and 15. The steady loading has minimal effect on the unsteady pressure magnitude data on either blade surface with both surfaces showing nearly identical constant magnitude vs chord distribution for all three steady loading levels. The phase data chordwise trends are also unaffected by steady loading, but the data increase in level slightly with increased loading. A wave speed of approximately 320 m/s on each surface of the rotor blade is calculated from the linear, constant slope, chordwise distributions of these phase data. This corresponds to the speed of propagation of an upstream traveling acoustic wave, i.e., the speed of sound minus the axial velocity. Since the unsteady pressure magnitude and phase chordwise distributions are nearly identical for both the pressure surface and suction surface, the unsteady pressure difference distribution across the blade is nearly zero. Therefore, the unsteady lift due to acoustic waves is also nearly zero.

Summary and Conclusions

The effects of steady aerodynamic loading on the first harmonic unsteady gust aerodynamics of a first-stage rotor blade at realistic high values of the reduced frequency were investigated and quantified. This was accomplished by means of a series of experiments performed in an extensively instrumented axial flow research compressor with the high-reduced frequency gusts generated by the wakes from the IGV. The analysis of these rotor-blade surface steady and unsteady data determined the following.

1) Steady loading affects the rotor-blade, static pressure distributions on the front portion of the pressure surface and over the entire suction surface with no steady flow separation indicated.

2) The unsteady pressure response on the blade pressure surface, i.e., the low-camber surface, is primarily affected by the level of steady loading as characterized by the mean flow incidence angle except in the accelerating mean flowfield of the front chord region at negative mean flow incidence.

3) The unsteady pressure response on the high-camber blade suction surface is affected by the level of steady loading, i.e., the accelerating mean flowfield in the front half of the surface and the large viscous regions in the aft half of the surface.

4) The unsteady pressure difference data reflect the effects of loading on the pressure and suction surface unsteady data with the suction surface effects being dominant.

5) These steady loading effects cause the chordwise distribution of the magnitude and phase data to differ greatly from the flat plate cascade predictions. A super-resonant condition was also established in the compressor, accomplished by altering the number of vanes in each downstream stator row. This resulted in a relatively large amplitude upstream propagating acoustic wave generated by the downstream rotor-stator row interactions.

6) In the leading-edge region of the first-stage, rotor-blade row suction surface, the acoustic wave has an amplitude approximately one-fourth that of the first harmonic of the IGV wakes.

7) Loading has minimal effect on the resulting rotor-blade surface acoustic wave generated unsteady pressure data with the only effect being a slight phase increase with increased steady loading.

8) Since the unsteady pressure chordwise magnitude and phase distributions are nearly identical for both the pressure

and suction surfaces, the unsteady pressure difference across the blade and, thus, unsteady lift, due to acoustic waves is nearly zero.

Acknowledgments

Research was sponsored by the Air Force Office of Scientific Research under Contract F49620-88-C-0022.

References

[1]Sears, W. R., "Some Aspects of Non-Stationary Airfoil Theory and its Practical Application," *Journal of Aeronautical Sciences,* Vol. 8, No. 3, 1941, pp. 104-108.

[2]Whitehead, D. C., "Force and Moment Coefficients for Vibrating Airfoils in Cascade," British Aeronautical Research Council, London, ARC R&M 3254, Feb. 1960.

[3]Fleeter, S., "Fluctuating Lift and Moment Coefficients for Cascaded Airfoils in Nonuniform Compressible Flow," *Journal of Aircraft,* Vol. 10, No. 2, Feb. 1973, pp. 93-98.

[4]Smith, S. N., "Discrete Frequency Sound Generation in Axial Flow Turbomachines," British Aeronautical Research Council, London, ARC R&M 3709, 1971.

[5]Goldstein, M. E., and Atassi, H., "A Complete Second-Order Theory for the Unsteady Flow about an Airfoil due to a Periodic Gust," *Journal of Fluid Mechanics,* Vol. 74, 1976, pp. 741-766.

[6]Atassi, H. M., "The Sears Problem for a Lifting Airfoil Revisited-New Results," *Journal of Fluid Mechanics,* Vol. 141, 1984, pp. 109-122.

[7]Chiang, H. D., and Fleeter, S., "Prediction of Loaded Airfoil Unsteady Aerodynamic Gust Response by a Locally Analytical Method," *International Journal of Mathematical Modeling,* Vol. 10, No. 3, 1988, pp. 193-206.

[8]Fleeter, S., Jay, R. L., and Bennett, W. A., "Rotor Wake Generated Unsteady Aerodynamic Response of a Compressor Stator," *ASME Journal of Engineering for Power,* Vol. 100, Oct. 1978, pp. 664-675.

[9]Fleeter, S., Jay, R. L., and Bennett, W. A., "Wake Induced Time Variant Aerodynamics Including Rotor-Stator Axial Spacing Effects," *ASME Journal of Fluids Engineering,* Vol. 103, No. 1, March 1981, pp. 59-66.

[10]Capece, V. R., Manwaring, S. R., and Fleeter, S., "Unsteady Blade Row Interactions in a Multi-Stage Compressor," *Journal of Propulsion and Power,* Vol. 2, No. 2, 1986, pp. 168-174.

[11]Capece, V. R., and Fleeter, S., "Unsteady Aerodynamic Interactions in a Multi-Stage Compressor," *ASME Journal of Turbomachinery,* Volume 109, No. 3, July 1987, pp. 420-428.

[12]Hardin, L. W., Carta, F. O., and Verdon, J. M., "Unsteady Aerodynamic Measurements on a Rotating Compressor Blade Row at Low Mach number," *ASME Journal of Turbomachinery,* Vol. 109, No. 4, Oct. 1987, pp. 499-507.

[13]Lakshminarayana, B., and Davino, R., "Mean Velocity and Decay Characteristics of the Guidevane and Stator Blade Wake of an Axial Flow Compressor," American Society of Mechanical Engineers, New York, ASME Paper 79-GT-9, April 1979.

[14]Hodson, H. P., "Measurement of the Wake-Generated Unsteadiness in the Rotor Passages of Axial-Flow Turbines," American Society of Mechanical Engineers, New York, ASME Paper 84-GT-189, June 1984.

[15]Carta, F. O., "Aeroelasticity and Unsteady Aerodynamics," *The Aerothermodynamics of Aircraft Gas Turbine Engines*, edited by G. Oates, Air Force AeroPropulsion Lab, AFAPL-TR-78-52, July 1978, pp. 22-1-22-54.